Advances in Applied Mathematics and Mechanics
Adv. Appl. Math. Mech., Vol. **9**, No. 5, pp. 1111-1132

DOI: 10.4208/aamm.OA-2016-0084
October 2017

A Comparison Study of Numerical Methods for Compressible Two-Phase Flows

Jianyu Lin[1], Hang Ding[1,*], Xiyun Lu[1] and Peng Wang[2]

[1] *Department of Modern Mechanics, University of Science and Technology of China, Hefei, Anhui 230026, China*
[2] *Institute of Applied Physics and Computational Mathematics, Beijing 100088, China*

Received 8 August 2016; Accepted (in revised version) 20 October 2016

Abstract. In this article a comparison study of the numerical methods for compressible two-phase flows is presented. Although many numerical methods have been developed in recent years to deal with the jump conditions at the fluid-fluid interfaces in compressible multiphase flows, there is a lack of a detailed comparison of these methods. With this regard, the transport five equation model, the modified ghost fluid method and the cut-cell method are investigated here as the typical methods in this field. A variety of numerical experiments are conducted to examine their performance in simulating inviscid compressible two-phase flows. Numerical experiments include Richtmyer-Meshkov instability, interaction between a shock and a rectangle SF_6 bubble, Rayleigh collapse of a cylindrical gas bubble in water and shock-induced bubble collapse, involving fluids with small or large density difference. Based on the numerical results, the performance of the method is assessed by the convergence order of the method with respect to interface position, mass conservation, interface resolution and computational efficiency.

AMS subject classifications: 76E17, 76L05, 76T10

Key words: Diffuse interface method, modified ghost fluid method, cut-cell method, compressible flow, two-phase flow.

1 Introduction

In past decades a variety of numerical methods have been developed for simulation of inviscid compressible two-phase flow. Since these methods allow for complicated interface deformations or topology changes of interfaces, they have been extensively used to investigate the high-speed flows involving shock-interface interactions, and therefore become

*Corresponding author.
Email: linjiany@mail.ustc.edu.cn (J. Y. Lin), hding@ustc.edu.cn (H. Ding), xlu@ustc.edu.cn (X. Y. Lu), wangpei@iapcm.ac.cn (P. Wang)

powerful numerical tools to elucidate the underlying fluid mechanisms. In these methods it is the key issue to appropriately deal with the jump conditions at the fluid-fluid interfaces. Depending on the manner of modeling the interface, the numerical methods can be generally grouped into two types: diffuse interface methods and sharp interface methods.

In the diffuse interface methods [1–7] the interface between two immiscible fluids is modeled by an interface region of finite thickness, in which the fluids are allowed to mix to some extent. For the fluid mixture in the diffuse interface region, it is very important to give consistent thermodynamic laws [3], which essentially resolve the jump conditions at the interface. The interface in the diffuse interface method can be represented by the field of different parameters, e.g., mass fraction [2], volume fraction [4] or specific heat ratio [8]. In order to reflect the discontinuous nature of the immiscible fluids, the thickness of the diffuse interface is supposed to be much smaller than the characteristic length scale of the flow. However, the non-uniform flow field would stretch or compress the diffuse interface region. How to suppress the interface diffusion remains a big challenge in the diffuse interface simulation of compressible multiphase flows, and recent efforts can be found in [9–14].

In the sharp interface methods the interface is treated as a sharp contact discontinuity. Two typical sharp interface methods on Cartesian meshes are: ghost fluid methods [15–19] and cut-cell methods [20, 21]. The ghost fluid methods generally resolve the fluid flows in the finite difference framework, in particular at the Cartesian cells that contain the interface, where the discretization of governing equation in one fluid requires the information of the flow variables at the cells in the other fluid (or *ghost cells*). It is suggested by Fedkiw et al. [15] that the pressure and velocity can be copied from the other fluid directly while the density is obtained by extrapolating entropy from the side of the bulk fluid. Liu et al. [16] proposed a modified ghost fluid method, which includes a Riemann solver in the calculation of the flow variables at the ghost cells, to provide a non-oscillatory pressure field in the presence of strong shock and detonation waves at the interface. In the cut cell methods complex interfaces are projected onto a fixed structured mesh, and for two-dimensional computations the interface can be effectively represented by a number of piecewise linear segments that split the corresponding Cartesian cells. Consequently, a set of unstructured cells are generated in the vicinity of the interface [21–23]. Therefore, the interface coincides with the cell faces of the unstructured cells, and the jump conditions across the interface can be resolved by solving a local Riemann problem at the cell faces. In order to generate unstructured interface cells and eliminate the unnecessarily small ones, cut-cell methods often involve with complicated geometrical algorithms to split Cartesian cells and merge unstructured cells [23]. For the sharp interface methods, the interface evolution can be modeled by any popular interface tracking methods such as level-set [15], front tracking [19] and volume-of-fluid [24].

Despite of their success in simulating inviscid compressible two-phase flows, these methods have not been systematically compared yet, and therefore, it is not clear for a particular method about its advantages and disadvantages relative to the other ones.

In this paper, we choose the transport five equation model [4] as a typical diffuse interface method, and the modified ghost fluid method [18] and the cut-cell method [25] as the candidates for the sharp interface methods. A variety of numerical experiments are conducted to examine the performance of the three methods in simulating inviscid compressible two-phase flows, in the presence of small or large density difference. They include Richtmyer-Meshkov instability, interaction between a shock and a rectangle SF_6 bubble, Rayleigh collapse of a cylindrical gas bubble in water and shock-induced bubble collapse. Based on the numerical results, the performance of the method is assessed by the convergence order of the method with respect to interface position, mass conservation, interface resolution and computational efficiency.

The paper is organized as follows: a brief review of the three methods is given in Section 2, followed by code validation in Section 3. The numerical experiments are provided in Section 4, along with the performance discussion of the three different methods. Concluding remarks are addressed in Section 5.

2 Methodology

We consider here numerical simulations of inviscid two-phase flows, of which the motion is governed by Euler equations,

$$\frac{\partial \mathbf{Q}}{\partial t}+\nabla\cdot\mathbf{F}=\mathbf{0}, \tag{2.1}$$

in which the conservative variables $\mathbf{Q}$ and the flux function $\mathbf{F}$ are defined in a different way for the diffuse interface methods and the sharp interface methods.

2.1 Transport five equation model

We introduce here the typical diffuse interface method, i.e., the transport five equation model (TFEM) [4], for simulating two inviscid compressible fluids 1 and 2. The densities of the fluids are ρ_1 and ρ_2, respectively. In the interface region the two fluids are allowed to mix to some degree, and it is assumed that the density of the mixed fluid follows $\rho=\rho_1\alpha+\rho_2(1-\alpha)$, the flow velocity $\mathbf{u}=\mathbf{u}_1=\mathbf{u}_2$, the pressure $p=p_1=p_2$, the specific total energy $E=\epsilon+\frac{1}{2}\mathbf{u}^2$, and the specific inner energy $\epsilon=(\rho_1\alpha\epsilon_1+\rho_2(1-\alpha)\epsilon_2)/\rho$, where the subscript 1 and 2 indicate the respective fluid and α is the volume fraction of the fluid 1. In such a way, $\mathbf{Q}$ and $\mathbf{F}$ can be written as,

$$\mathbf{Q}=\begin{pmatrix}\rho_1\alpha\\ \rho_2(1-\alpha)\\ \rho u\\ \rho v\\ \rho E\end{pmatrix},\quad \mathbf{F}=\begin{pmatrix}\rho_1\alpha u\mathbf{i}+\rho_1\alpha v\mathbf{j}\\ \rho_2(1-\alpha)u\mathbf{i}+\rho_2(1-\alpha)v\mathbf{j}\\ (\rho uu+p)\mathbf{i}+\rho uv\mathbf{j}\\ \rho uv\mathbf{i}+(\rho vv+p)\mathbf{j}\\ (\rho E+p)u\mathbf{i}+(\rho E+p)v\mathbf{j}\end{pmatrix}.$$

The flow velocity $\mathbf{u}=(u, v)$, and $\mathbf{i}$ and $\mathbf{j}$ denote the unit vector in the x and y-direction, respectively. The evolution of the interface between the fluids 1 and 2 can be modelled by time variation of α, which obeys:

$$\frac{\partial \alpha}{\partial t}+\mathbf{u}\cdot\nabla\alpha=0. \tag{2.2}$$

To complete the system, the stiffened gas model is chosen to be the equation of states for each fluid:

$$p_i+\gamma_i\pi_i=(\gamma_i-1)\rho_i\epsilon_i, \tag{2.3}$$

where the subscript i (=1 or 2) denotes the respective fluid. Consequently, the equation of states for the fluid mixture at the interface region can be obtained:

$$p+\gamma\pi=(\gamma-1)\rho\epsilon, \tag{2.4}$$

where the specific heat ratio γ and the material-dependent constant π of the fluid mixture can be calculated by

$$\frac{1}{\gamma-1}=\frac{\alpha}{(\gamma_1-1)}+\frac{(1-\alpha)}{(\gamma_2-1)}, \tag{2.5a}$$

$$\frac{\pi\gamma}{\gamma-1}=\frac{\alpha\pi_1\gamma_1}{(\gamma_1-1)}+\frac{(1-\alpha)\pi_2\gamma_2}{(\gamma_2-1)}. \tag{2.5b}$$

In the present study the parameters are chosen as: for air $\gamma_a=1.4$ and $\pi_a=0$Pa, and for water $\gamma_w=4.4$ and $\pi_w=6\times10^8$Pa. The Eqs. (2.1) and (2.2) are solved by a 2nd finite volume method with the HLLC type scheme [8]. Eq. (2.2) can be rewritten as

$$\frac{\partial \alpha}{\partial t}+\nabla\cdot(\alpha\mathbf{u})=\alpha\nabla\cdot\mathbf{u}, \tag{2.6}$$

which can be numerically discretized as

$$\begin{aligned}&\frac{\mathrm{d}\alpha_{i,j}}{\mathrm{d}t}+\left(\frac{1}{\Delta x}((\alpha u)_{i+1/2,j}-(\alpha u)_{i-1/2,j})+\frac{1}{\Delta y}((\alpha v)_{i,j+1/2}-(\alpha v)_{i,j-1/2})\right)\\ =&\alpha_{i,j}\left(\frac{1}{\Delta x}(u_{i+1/2,j}-u_{i-1/2,j})+\frac{1}{\Delta y}(v_{i,j+1/2}-v_{i,j-1/2})\right).\end{aligned} \tag{2.7}$$

Note that the numerical fluxes αu and αv are solved by a HLLC Riemann solver, whereas the velocity at the cell faces on the RHS of Eq. (2.7) is solved by the adapt-HLLC solver. More precisely, the velocity can be obtained by,

$$u_{i+1/2,j}=\frac{1+sign(s^*)}{2}\left[u^{\mathrm{L}}+s^-(\chi^{*\mathrm{L}}-1)\right]+\frac{1-sign(s^*)}{2}\left[u^{\mathrm{R}}+s^+(\chi^{*\mathrm{R}}-1)\right], \tag{2.8}$$

where $s^-=\min(0,s^{\mathrm{L}})$, $s^+=\max(0,s^{\mathrm{R}})$, $\chi^{*\mathrm{L}}=(s^{\mathrm{L}}-u^{\mathrm{L}})/(s^{\mathrm{L}}-s^*)$, $\chi^{*\mathrm{R}}=(s^{\mathrm{R}}-u^{\mathrm{R}})/(s^{\mathrm{R}}-s^*)$, and

$$s^{\mathrm{L}}=\min\left((u-c)^{\mathrm{ROE}},u^{\mathrm{L}}-c^{\mathrm{L}}\right),\qquad s^{\mathrm{R}}=\max\left((u+c)^{\mathrm{ROE}},u^{\mathrm{R}}-c^{\mathrm{R}}\right), \tag{2.9}$$

where c is the sound speed, the superscripts L and R denote the left- and right-hand sides of the edge respectively, and the superscript ROE stands for the Roe average [26]. The intermediate wave speed s^* is computed by,

$$s^*=\frac{p^{\mathrm{R}}-p^{\mathrm{L}}+\rho^{\mathrm{L}}u^{\mathrm{L}}(s^{\mathrm{L}}-u^{\mathrm{L}})-\rho^{\mathrm{R}}u^{\mathrm{R}}(s^{\mathrm{R}}-u^{\mathrm{R}})}{\rho^{\mathrm{L}}(s^{\mathrm{L}}-u^{\mathrm{L}})-\rho^{\mathrm{R}}(s^{\mathrm{R}}-u^{\mathrm{R}})}. \tag{2.10}$$

2.2 Sharp interface methods

In this section we give a brief review of two sharp interface methods: the ghost fluid method [18] and the cut-cell method [25]. In both methods $\mathbf{Q}$ and $\mathbf{F}$ are defined as:

$$\mathbf{Q}=\begin{pmatrix}\rho\\ \rho u\\ \rho v\\ \rho E\end{pmatrix},\quad \mathbf{F}=\begin{pmatrix}\rho u\mathbf{i}+\rho v\mathbf{j}\\ (\rho uu+p)\mathbf{i}+\rho uv\mathbf{j}\\ \rho uv\mathbf{i}+(\rho vv+p)\mathbf{j}\\ (\rho E+p)u\mathbf{i}+(\rho E+p)v\mathbf{j}\end{pmatrix}.$$

A level set method is used to track the interface by means of the signed distance function ϕ, of which the time evolution follows:

$$\frac{\partial\phi}{\partial t}+\mathbf{v}\cdot\nabla\phi=0, \tag{2.11}$$

in which the interface velocity $\mathbf{v}$ is used to advance the ϕ field, rather than the flow velocity $\mathbf{u}$. Here, $\mathbf{v}$ is extended from the solution of a local Riemann problem at the interface along the normal direction of interface.

To keep ϕ as the signed distance function during the computation, a high-order reinitialization method [27] is implemented in each time step:

$$\frac{\partial\phi}{\partial t}+\frac{\tilde{\phi}}{\sqrt{\tilde{\phi}^2+\Delta x^2}}\left(\sqrt{\left(\frac{\partial\phi}{\partial x}\right)^2+\left(\frac{\partial\phi}{\partial y}\right)^2}-1\right)=0.5F, \tag{2.12}$$

where $\tilde{\phi}$ is level-set function before the re-initialization process, and F is a source term. Following the work of Hartmann et al. [27], F at the cell (i,j) is defined as

$$F_{i,j}=\frac{1}{\Delta x}\left(\frac{1}{\mathrm{M}_{i,j}}\sum_{k=1}^{\mathrm{M}_{i,j}}\frac{\tilde{\phi}_{i,j}}{\tilde{\phi}_{(i,j)_k}}\phi_{(i,j)_k}-\phi_{i,j}\right), \tag{2.13}$$

where $\tilde{\phi_{i,j}}\tilde{\phi}_{(i,j)_k}<0$, $\phi_{i,j}\phi_{(i,j)_k}<0$ and $\mathrm{M}_{i,j}$ is the number of the cells with the opposite sign of level-set function in the immediate neighborhood of the cell (i,j).

For the spatial discretization of the advection and reinitialization of the level-set function, i.e., Eq. (2.11) and Eq. (2.12), we use a fifth-order HJWENO finite-difference scheme [28]. For the temporal discretization, we use a second-order Runge-Kutta method for the advection of the level set equation Eq. (2.11) and a third-order Runge-Kutta scheme for the reinitialization Eq. (2.12) [30]. The Euler equations are solved by a 2$^{\mathrm{nd}}$ finite volume method (FVM) with HLL scheme [29].

2.2.1 Ghost fluid method

In the ghost fluid methods [15, 16], the Cartesian cells are classified according to the interface position, so that each cell is occupied by one particular fluid. In this way, the governing equations for single phase flows (e.g., Eq. (2.1)) are solved at every Cartesian cell. At the Cartesian cell in the immediate neighborhood of the interface, the discretization needs the information of the flow variables in the corresponding ghost cells, i.e., the cells in the other fluid. The essence of ghost fluid method is that the flow values at the ghost cells are populated appropriately so that the jump condition across the interface is satisfied. In such a way, numerical schemes can be directly applied at the cells near the interface. In present study we use the modified ghost fluid method (MGFM) [18]. The Riemann problem is first constructed at the interface, and then is solved by an exact Riemann solver [18]. The resultant solutions of the Riemann problem are employed to fill the ghost region.

Fig. 1 illustrates an example of constructing the local Riemann problem at the interface and the way of populating the ghost region (for fluid 1 in particular). For an arbitrary cell (i,j) in fluid 1 (i.e., $\phi<0$), if any of its neighboring cells, i.e., $(i+1,j)$, $(i-1,j)$, $(i,j-1)$ and $(i,j+1)$, is located in fluid 2, the cell (i,j) is considered to be an interface cell of fluid 1. As a result, a local Riemann problem shall be constructed at this cell. For convenience, the left and right states of the Riemann problem, i.e., density, pressure and the velocity component normal to the interface are defined as ρ_L, p_L, u_{nL} and ρ_R, p_R, u_{nR}, respectively. For the interface cell K in Fig. 1, the left and right states are approximated through a bilinear interpolation at the positions $\mathbf{x}_L$ and $\mathbf{x}_R$, respectively. Mathematically, $\mathbf{x}_L$ and $\mathbf{x}_R$ can be computed by $\mathbf{x}_L=\mathbf{x}_{IK}-1.5\Delta x\mathbf{n}_K$ and $\mathbf{x}_R=\mathbf{x}_{IK}+1.5\Delta x\mathbf{n}_K$, where $\mathbf{x}_{IK}=\mathbf{x}_K-\phi_K\mathbf{n}_K$

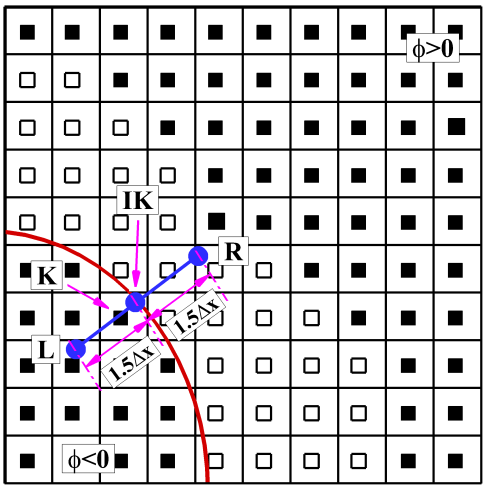

Figure 1: Construction of local Riemann problem for cell K in fluid one ($\phi<0$) in MGFM. The red solid line represents the interface. The black or hollow square is the cell center. The hollow squares are within 4 level of cells near the interface in the ghost region of fluid one.

and $\mathbf{n}_K = \frac{\nabla\phi}{|\nabla\phi|}$ is the normal vector at cell K. By solving the Riemann problem the states at the left side of the interface are defined as $\mathbf{W}_L = (\rho_L^*, p_L^*, u_{nL}^*)$. The states at cell K are corrected by keeping the tangential velocity along the interface unchanged and using $\mathbf{W}_L$ to replace other variables. This correction at the interface cell can prevent the diffusion of the entropy field across the interface [18]. Finally, the states are extended along the normal direction of the interface into the ghost region of fluid one by,

$$\frac{\partial \mathbf{q}}{\partial \tau} + \mathbf{n} \cdot \nabla \mathbf{q} = 0, \tag{2.14}$$

where $\mathbf{q}$ are the primitive variables and τ is the virtual time. For the extension of fluid 2, $\mathbf{n}$ should be replaced by $-\mathbf{n}$ in Eq. (2.14). This equation is solved by a first-order upwind scheme within a narrow band with width 4 level of cells near the interface, as shown in Fig. 1. After the populating of the ghost region of fluid 1, the interface cells in fluid 1 can be solved by the traditional single-phase solver. Constructing and solving the Riemann problem at the interface cell of fluid 2 follow similar procedure, and so does the population of the ghost cells of fluid 2.

2.2.2 Cut-cell method

A cut-cell method (CCM) is proposed recently to simulate the inviscid compressible two-phase flows with topology change of fluid-fluid interface in the frame work of finite volume methods [25]. In CCM two meshes are adopted: the background structured Cartesian mesh and the overlaid unstructured mesh near the interface; the latter is the dynamically generated by the cut cell method to account for the moving interface. In each Cartesian cell that contains the interface, the interface is represented by the line segments, and the typical cut cells that occur in the linear reconstruction of interface in one Cartesian cell are shown in Fig. 2. The split Cartesian cells are combined and form unstructured interface cells, which contain at least one edge along the interface. One example to form the interface unstructured cells is shown in Fig. 3. In this way, the interface becomes a moving edge of unstructured interface cells, and finite volume method can be directly applied in the spatial discretization at these cells, with no need of ghost cells. The jump conditions at the interface edges are enforced through an exact solver of Riemann problem [18].

A second-order Runge-Kutta method [30] is used for the time integration of the Euler equations. Each integration step in this explicit scheme can be generally written in the following form,

$$\mathbf{Q}^{n+1}\Delta S^{n+1} - \mathbf{Q}^n \Delta S^n = -\Delta t \sum_e \mathbf{F_e}^n \Delta l_e^n, \tag{2.15}$$

where the subscript e denotes the cell faces, the superscripts n and $n+1$ represent the time level, and Δl_e represents the area of the corresponding cell face. $\mathbf{F_e}$ denotes the numerical

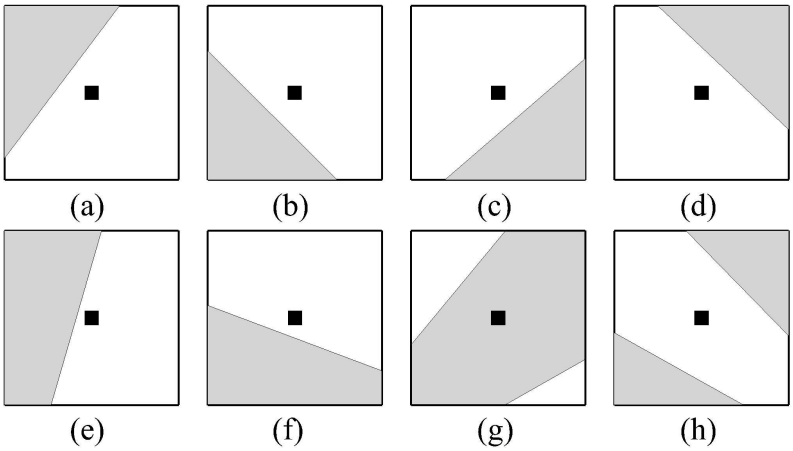

Figure 2: Typical cut cells that occur in the linear reconstruction of interface. The symbol ■ denotes the center of the Cartesian cell, and the gray color indicates the fluid 1 while the white color indicates the fluid 2.

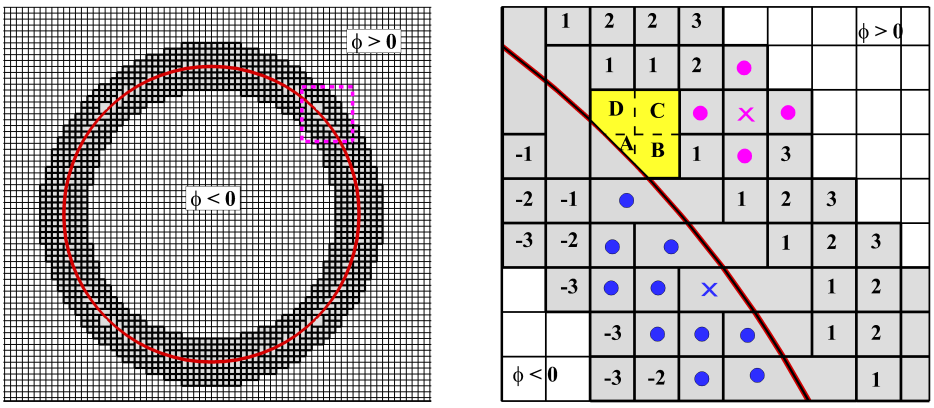

Figure 3: Left: A sample of Cartesian mesh (thin solid line) and unstructured mesh (bold solid line). Right: The zoomed figure in the dashed box in left frame. The red line in both frames represents the interface. In the right frame we also show the unstructured cells in the buffer layer which are labeled as level -1 to -3 in fluid one ($\phi<0$) and level 1 to 3 in fluid two ($\phi>0$). The interfacial unstructured cells may contain several subcells and one example is shown with 4 subcells marked as A∼D. The gradients of primitives on the unstructured cells are calculated with 2^{nd}least square method and the stencils for the interfacial unstructured cells (blue cross) and the unstructured cells in the buffer layer (pink cross) are shown by the blue and pink dots besides the cross it self.

flux estimated in the middle of cell faces [21], and is generally defined as

$$\mathbf{F_e}=\begin{pmatrix}\rho(U_n-U_b)\\ \rho u(U_n-U_b)+pn_x\\ \rho v(U_n-U_b)+pn_y\\ \rho E(U_n-U_b)+pU_n\end{pmatrix}, \tag{2.16}$$

where $U_n=\mathbf{u}\cdot\mathbf{n}_e$, $U_b=\mathbf{u}_b\cdot\mathbf{n}_e$, $\mathbf{u}_b$ is the velocity of the cell face, and $\mathbf{n}_e=(n_x,n_y)$ is the

normal vector of the cell face and points outwards. Note that $\mathbf{u}_b = 0$ for all the Cartesian cells, and it is non-zero only when the cell is an interface cell and the cell face coincides with the interface.

In the cut cell methods how to appropriately deal with the reinitialization process of the level set function is of great importance, particularly in the presence of interfaces with topology change or very high curvature, where the mesh is not sufficiently fine to resolve the interface. Traditionally the reinitialization equation Eq. (2.12) is calculated after the level-set equation immediately, but this treatment could give rise to significant unphysical oscillation of pressure [25]. Such problem could become worse in two-phase flows with large density ratio such gas-water flows, e.g., leading to the failure of the computation. The local unphysical oscillation of flow variables in the presence of topology change is shown to be greatly suppressed by using a delayed reinitialization [25]. As a result, the cut cell method can achieve second-order accuracy with respect to the interface position in the absence of topology changes of interface, while locally degrading to first-order at the interface region where topology change occurs. Another challenge is to eliminate the too small cut cells (e.g., of which the volume is less than $0.5\Delta x^2$), which results from the cutting of Cartesian cells by the interface. In practice, these small cut cells are merged with their neighbouring cells, in order to relieve the restriction of the time step arising from the explicit time-discretization scheme.

3 Validation

Two shock tube problems are considered here to validate our codes of TFEM, MGFM and CCM. Although they are one-dimensional flows, they are simulated by two-dimensional codes; the results only vary in the x-direction and are uniform in the y-direction.

3.1 Case A: gas-gas shock tube problem

The simulation configuration of gas-gas shock tube problem is set as follows: Initially, the flow properties of the gas between [0,0.5] m are: $\rho_L = 1\text{kg/m}^3$, $p_L = 10^5\text{Pa}$, $u_L = v_L = 0\text{m/s}$, $\gamma_L = 1.4$, while the gas in [0.5,1]m has: $\rho_R = 0.125\text{kg/m}^3$, $p_R = 10^4\text{Pa}$, $u_R = v_R = 0\text{m/s}$, $\gamma_R = 1.2$. The flow is simulated on uniform Cartesian meshes with 100 grids in the x-direction. All the boundaries are assumed to be slip solid walls, thus no-penetration boundary conditions are used. Since the results have no difference in the y-direction, we only show the distribution of the results along the x-direction only in Fig. 4 at $t = 0.0007\text{s}$, superimposed by the exact solution. It is clear that the numerical results are in agreement with the exact solution for all the three methods.

3.2 Case B: gas-water shock tube problem

One case studied by Liu et al. [16] is chosen to validate the three codes for two-phase flows with large density ratio. Initially, in the x-direction the gas between [0,0.4]m has:

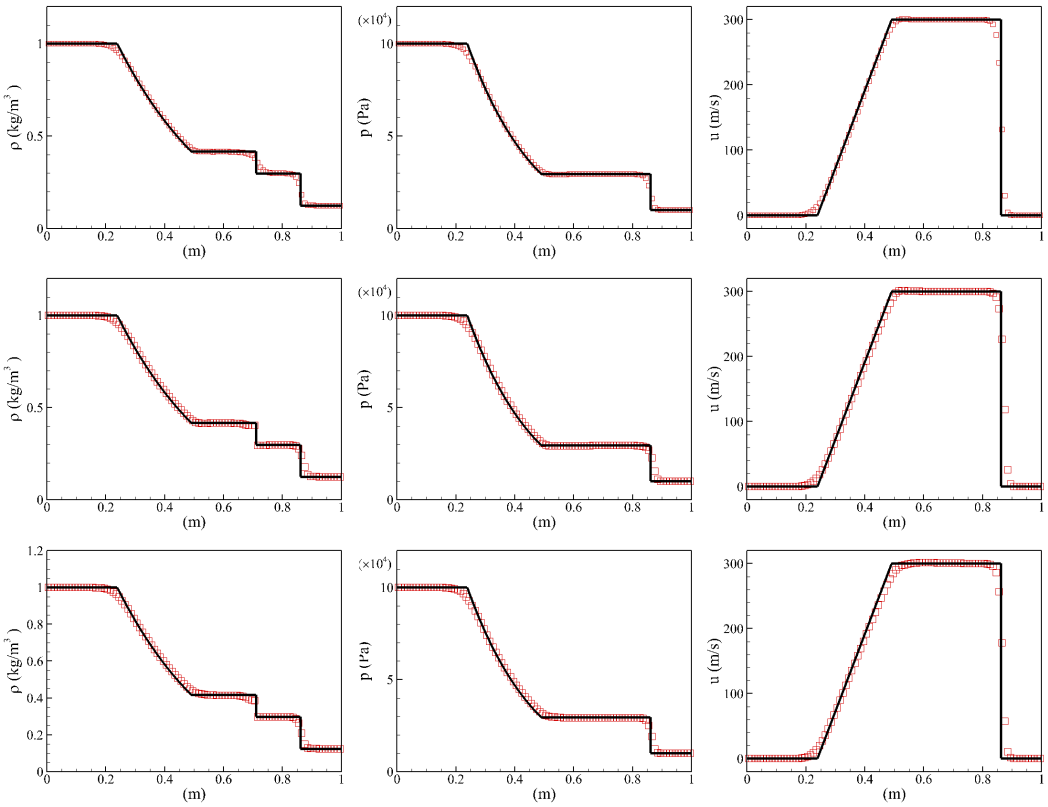

Figure 4: Numerical results at $t=0.0007$ s in the case A with respect to density (left column), pressure (middle column) and velocity (right column), using TFEM (upper row), MGFM (middle row) and CCM (bottom row), respectively.

$\rho_L=1\text{kg/m}^3$, $p_L=10^5\text{Pa}$, $u_L=100\text{m/s}$, $v_L=0\text{m/s}$, $\gamma_L=1.4$, while the water between [0.4,1]m has: $\rho_R=1000\text{kg/m}^3$, $p_R=2\times10^7\text{Pa}$, $u_R=v_R=0\text{m/s}$, $\gamma_R=4.4$, $\pi_R=6\times10^8\text{Pa}$. A Cartesian mesh with 200 grids in the x-direction are used here. All the boundaries are assumed to be slip solid walls. The results of TFEM, MGFM and CCM are shown in Fig. 5. This Riemann problem produces a left moving shock and a right moving rarefaction wave. It is shown that all the three code capture these waves, and the results agree well with the exact solutions.

4 Results and discussions

Unless mentioned otherwise, the CFL number is chosen to be 0.6, $\phi=0$ is used to show the interface position for MGFM and CCM, while $\alpha=0.5$ for TFEM.

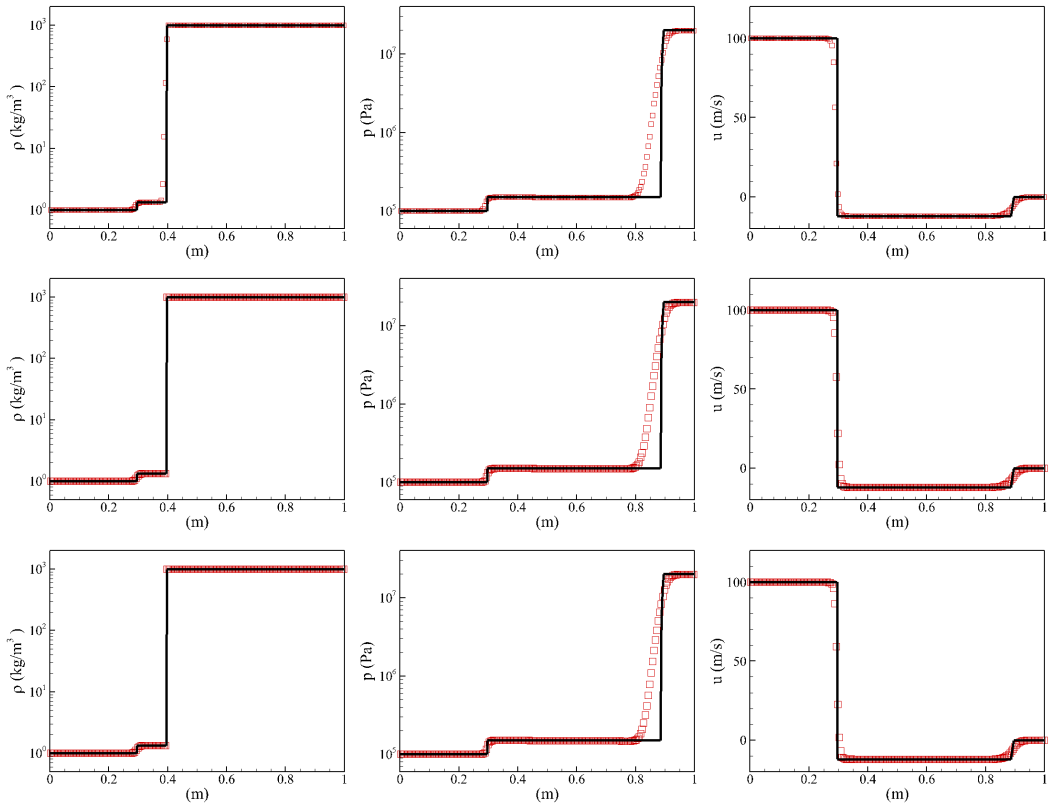

Figure 5: Numerical results at $t=0.0003$ s in the case B with respect to density (left column), pressure (middle column) and velocity (right column), using TFEM (upper row), MGFM (middle row) and CCM (bottom row), respectively.

4.1 Gas-gas flows

4.1.1 Richtmyer-Meshkov instability

We investigate here the Richtmyer-Meshkov instability (RMI) of single mode for the air-He interface [31, 32]. A schematic diagram of the numerical setup is shown in Fig. 6, in which a shock wave moves from the right side to the left side, and impinges on a sinusoidal interface with wavelength λ and amplitude a. The initial conditions of the flows are listed in Table 1. The shock Mach number M_s is 1.52, and the Atwood number A $(=(\rho_2-\rho_1)/(\rho_2+\rho_1))$ is set to 0.76, where ρ_1 denotes the density of air and ρ_2 is the density of He. Because of symmetry of the flows, only half of the domain is simulated. The size of the computational domain is $[-30,30]\times[0,2]$cm. Symmetric boundary condition is enforced at the up and bottom boundaries, and the extrapolation boundary condition is enforced at the left and right boundaries. The interface is initially placed at $x=-5$cm. The specific heat ratio γ is set to 1.4 for air and 1.63 for He. The mesh resolution is 480 cells per wavelength, and in the computation $t=0$ represents the moment when the inci-

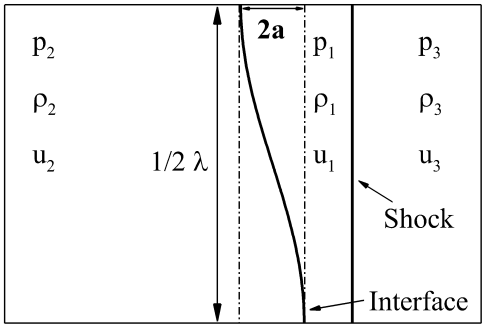

Figure 6: Numerical setup of RMI of single mode. λ is the wavelength of the interface perturbation and a is the amplitude.

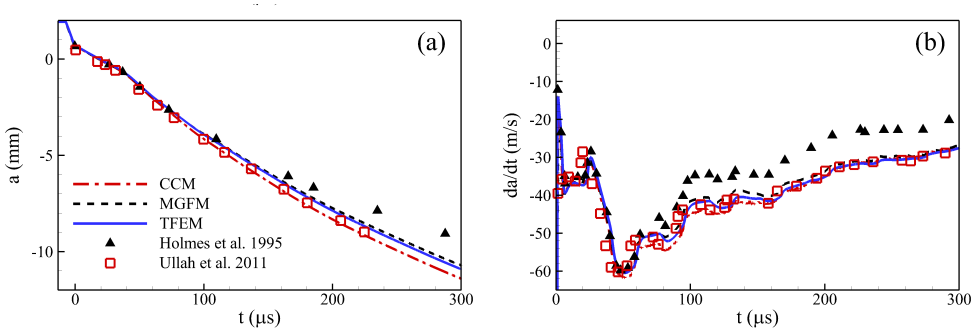

Figure 7: The time history of (a) amplitude and (b) growth rate in the Richtmyer-Meshkov instability of single mode of air-HE interface.

dent shock totally transmits the interface. To give a quantitative estimate of the interface deformation, we track the instantaneous amplitude of interfacial wave, $a(t)$, which is defined as half of the distance between the trough and the crest. Accordingly, we can also compute the growth rate $\mathrm{d}a(t)/\mathrm{d}t$.

Fig. 7 shows the time evolution of the amplitude and growth rate together with the numerical results from other researchers [31, 32]. Note that there are relatively big differences between the results of Holmes et al. [31] and Ullah et al. [32] with respect to the amplitude and the growth rate. Holmes et al. [31] adopt a non-conservative front track-

Table 1: Parameters for RMI of single mode. The units of pressure, density and velocity are bar, $\mathrm{kg/m^3}$ and m/s, respectively.

RMI of single mode for air-He interface		
$\lambda=4$cm and $a=0.2$cm		
$p_1=1.013$	$\rho_1=1.2$	$u_1=0$
$p_2=1.013$	$\rho_2=0.167$	$u_2=0$
$p_3=2.562$	$\rho_3=2.276$	$u_3=-246.977$

ing method, while Ullah et al. [32] use a conservative front tracking method. It appears that all our results are closer to those of Ullah et al. [32], regardless of the differences in the ways of dealing with interface conditions. A convergence study (not shown here) shows that such an observation is mesh independent.

4.1.2 Shock-SF_6 bubble interaction

We consider here the interaction between a shock and a rectangle SF_6 bubble in air. The initial setup is given in Fig. 8. The initial states in the SF_6 bubble are: $\rho_S = 5.805\text{kg/m}^3$, $p_S = 96856\text{Pa}$, $u_S = v_S = 0\text{m/s}$, $\gamma_S = 1.076$ and the states in air before the shock are: $\rho_a = 1.153\text{kg/m}^3$, $p_a = 96856\text{Pa}$, $u_a = v_a = 0\text{m/s}$, $\gamma_a = 1.4$. The states after the incident shock can be obtained by setting the shock Mach number to 1.26. A grid of 750×300 is used in the simulation. The extrapolation boundary condition is used at the left side boundary, and slip boundary conditions are adopted at the rest of the boundaries. $t = 0$ is set to the moment when the incident shock coincides with the left side of the SF_6 bubble.

Fig. 9 shows the snapshots of the experimental results obtained by Bates et al. [33]. It

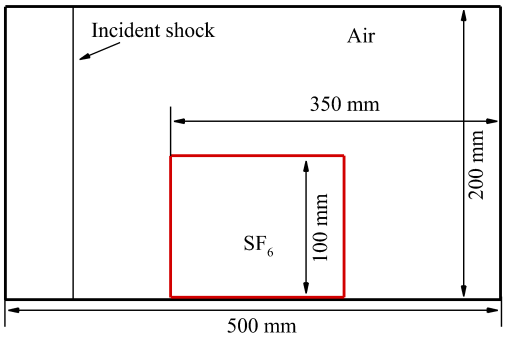

Figure 8: Setup for interactions between a shock and a rectangle block of SF_6.

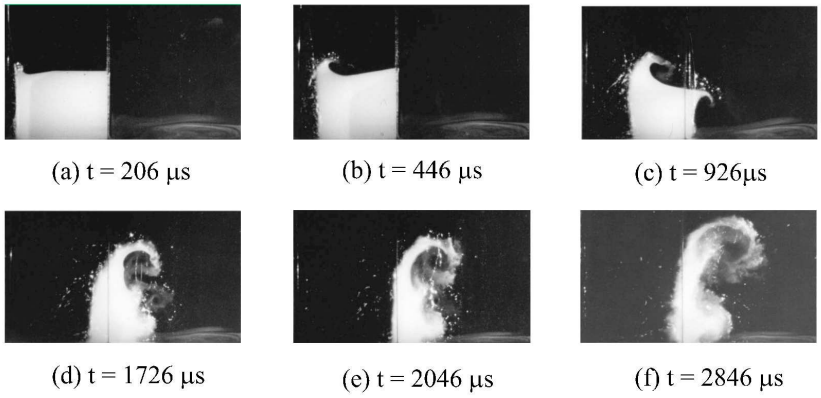

Figure 9: Experimental results of Bates et al. [33] in the interaction of shock and a rectangle $SF6_6$ bubble.

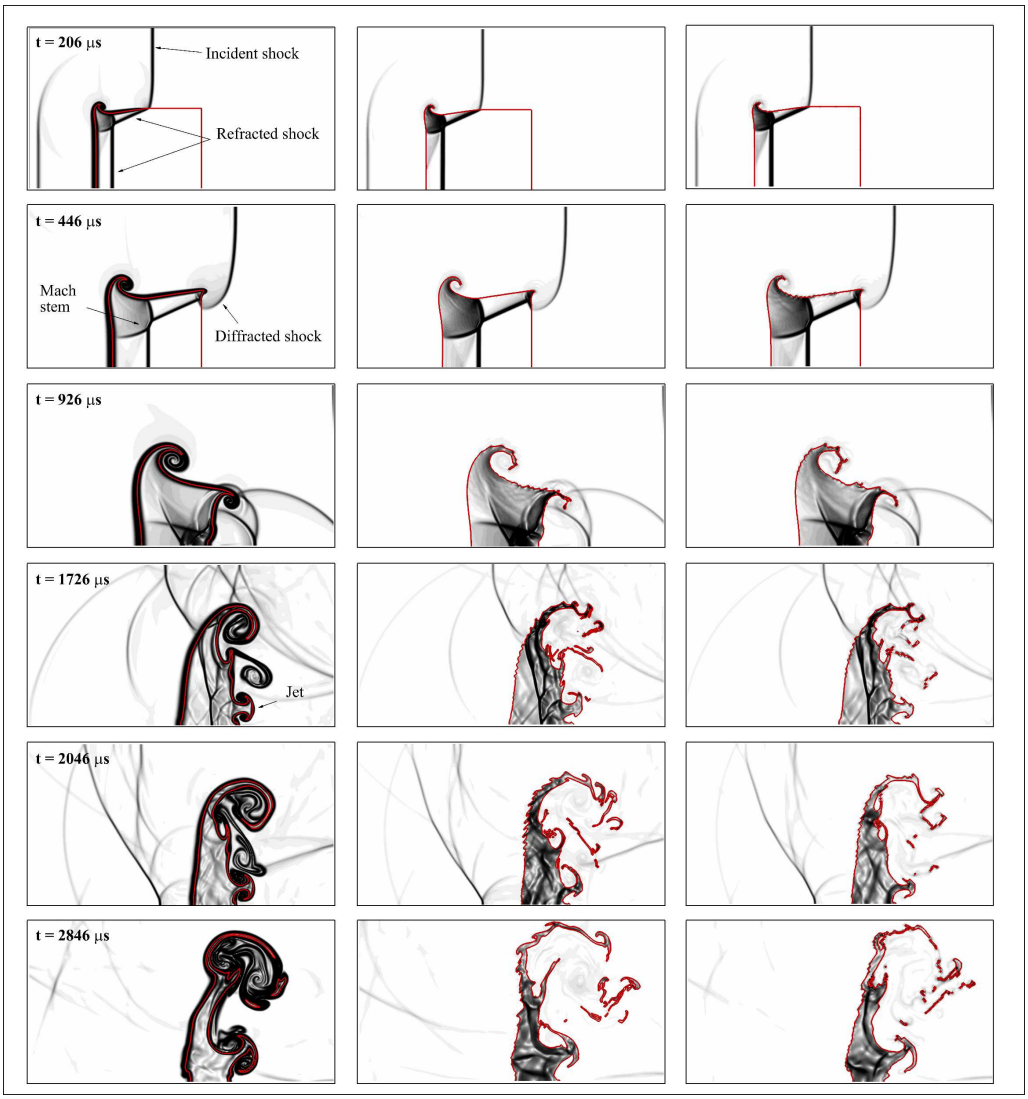

Figure 10: Numerical schlieren for TFEM (left column), MGFM (middle column) and CCM (right column). The red solid line is the contour of $\alpha=0.5$ in TFEM and $\phi=0$ in MGFM and CCM.

is clearly seen that the interface evolution exhbits significant deformation and breakups. Fig. 10 shows the numerical schlieren for TFEM, MGFM and CCM. Compared with the experiments, all the three methods are able to capture the main flow features. For example, when the shock impacts on the SF_6 bubble, the shock transmits into the SF_6 bubble to form the refracted shock, and at the same time the reflected shock wave is formed in the air. Along with the wave evolution, the baroclinic effect causes top-left corner of the SF_6 bubble to roll up, and a Mach stem occurs inside the SF_6 bubble to connect the two refracted shocks. A jet appears when this Mach stem impacts on the right side of the bub-

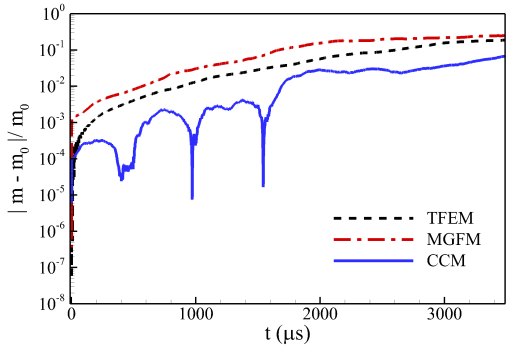

Figure 11: Relative error of mass versus time during the interaction between the shock and the SF_6 bubble. m_0 is the initial mass of the SF_6 bubble.

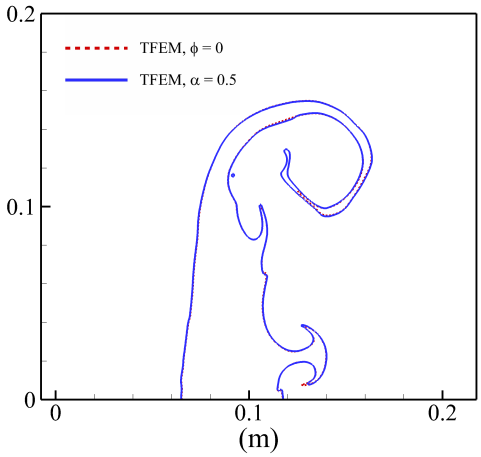

Figure 12: Interface shape at $t=2046\mu$s represented by $\phi=0$ and $\alpha=0.5$ with TFEM.

ble near the wall. Among the three numerical methods, sharp interface methods such as MGFM and CCM produce rather similar results, which have higher resolution than those of the diffuse interface method such as TFEM. On the other hand, the results of TFEM are smoother than those of MGFM and CCM, due to the effect of the mixture of the fluids.

The relative error of mass of the SF_6 bubble is shown in Fig. 11 as a function of time. We can see that the results of CCM have the smallest mass error among the three methods during the computation. In order to give an accurate prediction of the interface positions in TFEM, we make a comparison between the contour of $\alpha=0.5$ in TFEM and the level set function $\phi=0$ in Fig. 12. It should be noted that the level set function here is advected by the flow velocity obtained by TFEM, and does not couple with the computation of Euler equation. Thus, it can be viewed as a post-process of TFEM to determine the interface position. It is seen in Fig. 12 that the two results are virtually overlapped except for the under-resolved interface region. This observation implies that $\alpha=0.5$ is a good indication

in TFEM to represent the interface.

The computational efficiency is measured by the CPU time required at $t=2046\mu$s. In the computation we use the OpenMP to parallelize the code on a computer with 24 cores and 2.4GHz. In the present study, TFEM, MGFM and CCM cost 0.7, 2.0 and 2.2 hours, respectively. Since the reinitalization equation Eq. (2.12), the advection equation Eq. (2.14) and the local interfacial Riemann problems are solved in both MGFM and CCM, it is reasonably expected that such process would need longer computational time. Furthermore, the dynamic generation of the unstructured interface cells in the CMM also increases the computation load.

4.2 Gas-water flows

4.2.1 Rayleigh collapse

Rayleigh collapse refers to the symmetric collapse process of a gas bubble subject to a high pressure in the surrounding still fluid. The three methods are used to calculate the two-dimensional Rayleigh collapse in a domain [0,200] $\times$ [0,200]mm. A uniform mesh is used in [0,2] $\times$ [0,2]mm and stretched mesh is adopted in the other region. Initially an air bubble with radius $R_0=1$mm is placed at [0,0]mm and only a quarter of the bubble is calculated due to the symmetry. Slip boundary condition is enforced at the left and bottom boundaries while the extrapolation boundary condition is used at the others. The states inside the bubble are: p_0=10^5Pa, ρ=1kg/m^3, u=v=0m/s. The water outside is also at steady state with $\rho=1000$kg/m^3 and $p(r)=p_\infty+R_0(p_0-p_\infty)/r$, where r is the distance to the origin, $p_\infty=2\times10^7$Pa. These initial conditions are similar to the three-dimensional Rayleigh collapse studied by Tiwari et al. [12].

The effective radius is defined as R_e=$2(V/(\pi))^{1/2}$, where V is the volume of a quarter of bubble, and is shown in Fig. 13. It shows that all three methods are mesh convergent to the exact radius. The error of volume fraction is defined as [12]:

$$e_v=\frac{1}{N}\sum_{i,j}|\alpha_{i,j}-\alpha_e|, \tag{4.1}$$

where N is the total number of the cells, α_e is the exact volume fraction which is calculated from the one-dimensional cut-cell code for flow with cylindrical symmetry with 1600 points per radius. For CCM and TFEM, the volume fraction α can be obtained directly. However, for MGFM we use the same linear interface reconstruction technology to reconstruct the interface from the level-set function to get the volume fraction inside the cell as in CCM. Table 2 shows the error at $t=12\mu$s when the exact radius is 0.252710 mm. It can be seen that the convergence orders of TFEM, MGFM and CCM are roughly 0.6, 0.9 and 2, respectively. We must emphasize that the convergence orders are essentially obtained with respect to the interface position, and thus are related to the accuracy in dealing with the jump conditions, rather than the spatial discretization. In addition, it is also shown by Tiwari et al. [12] that the diffuse interface method achieves first-order accuracy at best in the numerical study of three-dimensional Rayleigh collapse.

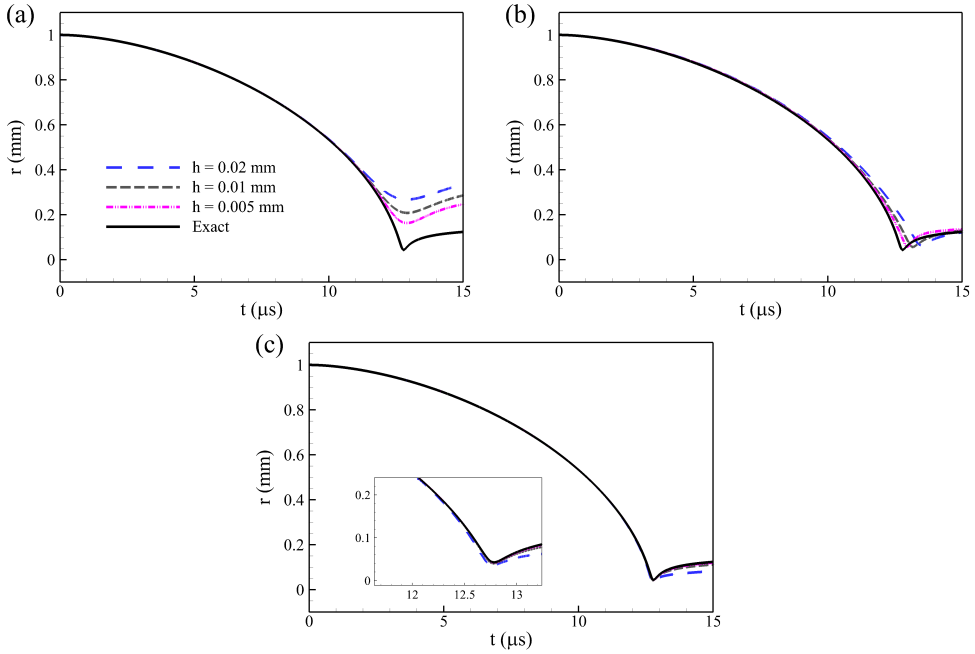

Figure 13: Effective radius versus time in two-dimensional Rayleigh collapse with TFEM (a), MGFM (b), CCM (c). The exact result is calculated by one-dimensional cut-cell code for flow with cylindrical symmetry with $h=0.000625$mm. The results near $t=12\mu$s is zoomed in the inset in (c).

4.2.2 Shock-induced bubble collapse

Shock-induced bubble collapse in water can be found in industrial applications such as shockwave lithotripsy [34], and has attracted the attentions of a lot of researchers [24, 35–38]. The case of bubble collapse induced by 1.9GPa shock is chosen to be the test case, and the results in [24, 37, 38] are chosen as the benchmark solutions. The density of the air bubble is $1\text{kg}/\text{m}^3$ and the pressure is 10^5Pa. The density of the water before the shock is $1000\text{kg}/\text{m}^3$. The computational domain has a size of $[-12,12]\times[0,12]$mm, with the bubble being centered at (0,0) mm initially. A hybrid structured mesh is used for discretization, in which a uniform mesh is placed in $[-5.6,6.4]\times[0,6.0]$mm while a stretched non-uniform mesh fills the rest of the domain. The reflection boundary is used at the lower boundary due to the symmetry of the flow, and the extrapolation boundary condition is used at the other boundaries. Three successively refined meshes (i.e., $h=0.03$mm, $h=0.015$mm and $h=0.0075$mm) in the uniform region are used. The finest resolution corresponds to 400 cells per radius of the bubble.

Fig. 14 shows the density and numerical schlieren with CCM. When the incident shock impacts on the bubble interface from the side of water, the shock is transmitted into the air, and at the same time rarefaction waves are reflected from the bubble interface. Due to the focusing of the flows, a jet forms at the upstream of the bubble. After the jet impacting on the downstream side of the bubble wall two water-hammer shocks are

Table 2: Error e_v at $t=12\mu$s in the 2-D Rayleigh collapse with different methods.

h(mm)	e_v for TFEM	order
0.02	2.26×10^{-3}	
0.01	1.46×10^{-3}	0.63
0.005	9.64×10^{-4}	0.60
h(mm)	e_v for MGFM	order
0.02	2.76×10^{-3}	
0.01	1.49×10^{-3}	0.89
0.005	7.81×10^{-4}	0.92
h(mm)	e_v for CCM	order
0.02	6.25×10^{-5}	
0.01	1.49×10^{-5}	2.07
0.005	3.47×10^{-6}	2.10

Table 3: Water-hammer shock pressure p_w, impact time t_c and maximum jet velocity v_j in the bubble collapse with different methods. Note that the impact time of Hawker&Ventikos [38] starts from the contact of the initial shock with the upstream bubble interface and in the bracket the time is transformed into the one which starts from the beginning of the computation as other results.

	h(mm)	TFEM	MGFM	CCM	Hawker [38]	Bo [24]	Nourgaliev et al. [37]
p_w(GPa)	0.03	4.07	5.33	4.94			
	0.015	4.31	5.37	5.47			
	0.0075	4.53	5.75	5.90	5.89		10.1
$t_c(\mu$s)	0.03	3.82	3.70	3.69			
	0.015	3.74	3.71	3.70			
	0.0075	3.72	3.71	3.70	2.8(3.66)	3.70	3.69
v_j(m/s)	0.03	2892	2816	2830			
	0.015	2870	2819	2828			
	0.0075	2850	2827	2832	2810	2830	2850

produced. One water-hammer shock moves to the upstream and the other moves to the downstream. At a later time a secondary jet is produced under the high pressure after the water-hammer shock as other researchers [24,37,38].

The bubble shapes at $t=4.1\mu$s are shown in Fig. 15 with three different meshes. It shows that both MGFM and CCM can capture the secondary jet even with only h=0.03mm but the secondary jet can only appear with the finest mesh when using TFEM. With the mesh refinement, CCM appears to converge faster than MGFM. Also, CCM can have a better resolution of the interface than MGFM, e.g., the bubble rim near the jet.

A quantitative comparison is provided in Table 3, in terms of the pressure after the water hammer shock, the maximum jet velocity and the time when the jet impacts the downstream interface of the bubble (namely impact time). In Table 3 the results of other researchers are all calculated with h=0.0075 mm. It shows that the impact time and maximum jet velocity using the three different methods only have insignificant difference.

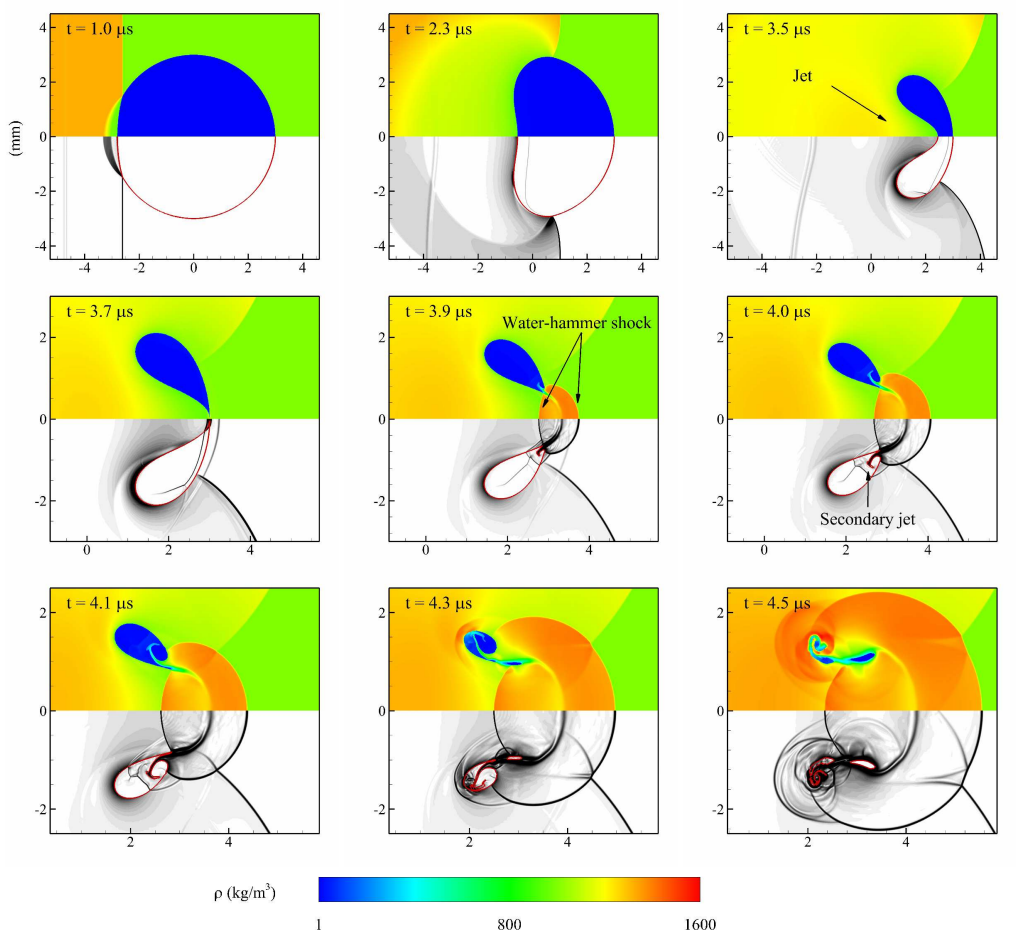

Figure 14: Density (above half) and numerical schlieren (below half) for shock-induced bubble collapse with CCM. The red lines represent the interface. The time is given in each frame.

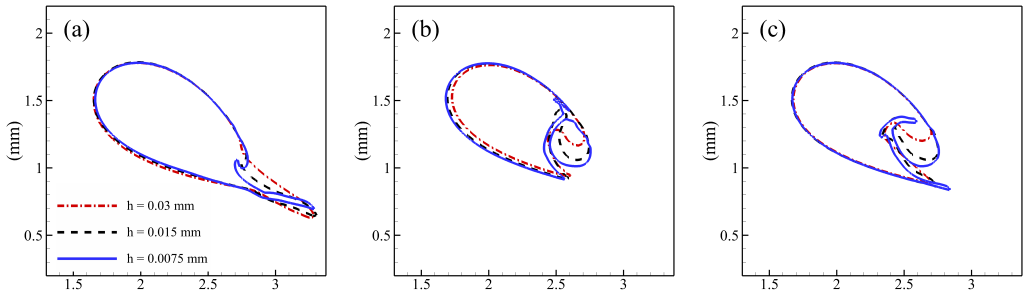

Figure 15: Bubble shapes at $t=4.1\mu$s with TFEM (a), MGFM (b), CCM (c).

Note that the impact time of Hawker&Ventikos [38] is smaller than that of all the other researchers and present work. The pressures after the water-hammer shock obtained by

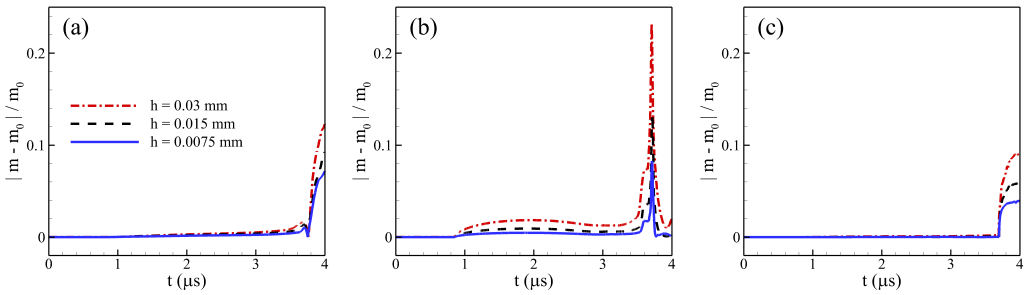

Figure 16: Relative mass error versus time with TFEM (a), MGFM (b), CCM (c).

MGFM and CCM are in good agreement with Hawker&Ventikos [38]; by contrast TFEM produces a water-hammer shock of a lower pressure. The relative error of mass of the air bubble is shown in Fig. 16 on the three different meshes. It shows that all the methods have smaller error with mesh refinement; the maximum errors at $h = 0.0075$mm are 7%, 8% and 4% for TFEM, MGFM and CCM, respectively. Note that a maximum error of 9% is reported by Bo&Grove [24] and 8% by Nourgaliev et al. [37]. CCM can maintain mass conservation before jet impacting, and overall has the least relative mass error among the three methods. Both TFEM and MGFM have relatively large errors, even before the occurrence of topology change.

5 Conclusions

In this study we make a comparison between one diffuse interface method, i.e., the transport five equation model (TFEM), and two sharp interface methods, i.e., the modified ghost fluid method (MGFM) and the cut-cell method (CCM), and systematically examine their performance in simulating inviscid compressible two-phase flows. The convergence study of the Rayleigh collapse problem shows that CCM can achieve second-order accuracy while TFEM and MGFM have first-order accuracy at best. The test of mass conservation suggests that CCM is superior to TFEM and MGFM. We also find that CCM obtains the best interface resolution on the same mesh among the three methods. On the other hand, TFEM requires the least computational cost among the three methods, and the computational efficiencies of MGFM and CCM are similar.

Acknowledgments

The authors would like to acknowledge the support of the Strategic Priority Research Program of the Chinese Academy of Sciences (Grant No. XDB22040103), the Science Challenge Program (Grant No. JCKY2016212A501) and the National Natural Science Foundation of China (Grant Nos. 11425210 and 11621202).

References

[1] R. ABGRALL, *How to prevent pressure oscillations in multicomponent flow calculations: A quasi conservative approach*, J. Comput. Phys., 125 (1996), pp. 150–160.

[2] K.-M. SHYUE, *An efficient shock-capturing algorithm for compressible multicomponent problems*, J. Comput. Phys., 142(1) (1998), pp. 208–242.

[3] R. SAUREL AND R. ABGRALL, *A multiphase Godunov method for compressible multifluid and multiphase flows*, J. Comput. Phys., 150(2) (1999), pp. 425–467.

[4] G. ALLAIRE, S. CLERC AND S. KOKH, *A five-equation model for the simulation of interfaces between compressible fluids*, J. Comput. Phys., 181(2) (2002), pp. 577–616.

[5] R. SAUREL, S. GAVRILYUK AND F. RENAUD, *A multiphase model with internal degrees of freedom: Application to shock-bubble interaction*, J. Fluid Mech., 495 (2003), pp. 283–321.

[6] A. MARQUINA AND P. MULET, *A flux-split algorithm applied to conservative models for multicomponent compressible flows*, J. Comput. Phys., 185(1) (2003), pp. 120–138.

[7] C.-H. CHANG AND M.-S. LIOU, *Robust and accurate approach to computing compressible multiphase flow: Stratified flow model and AUSM$^+$-up scheme*, J. Comput. Phys., 225(1) (2007), pp. 840–873.

[8] T. JOHNSEN AND E. COLONIUS, *Implementation of WENO schemes in compressible multicomponent flow problems*, J. Comput. Phys., 219(4) (2006), pp. 715–732.

[9] S. KOKH AND F. LAGOUTIÈRE, *An anti-diffusive numerical scheme for the simulation of interfaces between compressible fluids by means of a five-equation model*, J. Comput. Phys., 229(8) (2010), pp. 2773–2809.

[10] R. K. SHUKLA, C. PANTANO AND J. B. FREUND, *An interface capturing method for the simulation of multi-phase compressible flows*, J. Comput. Phys., 229(19) (2010), pp. 7411–7439.

[11] K. K. SO, X. Y. HU AND N. A. ADAMS, *Anti-diffusion interface sharpening technique for two-phase compressible flow simulations*, J. Comput. Phys., 231(11) (2012), pp. 4304–4323.

[12] A. TIWARI, J. B. FREUND AND C. PANTANO, *A diffuse interface model with immiscibility preservation*, J. Comput. Phys., 252 (2013), pp. 290–309.

[13] R. K. SHUKLA, *Nonlinear preconditioning for efficient and accurate interface capturing in simulation of multicomponent compressible flows*, J. Comput. Phys., 276 (2014), pp. 508–540.

[14] M. DELIGANT, M. SPECKLIN AND S. KHELLADI, *A naturally anti-diffusive compressible two phases Kapila model with boundedness preservation coupled to a high order finite volume solver,* Comput. Fluids, 114 (2015), pp. 265–273.

[15] R. P. FEDKIW, T. ASLAM, B. MERRIMAN AND S. OSHER, *A non-oscillatory Eulerian approach to interfaces in multimaterial flows (the ghost fluid method)*, J. Comput. Phys., 152(2) (1999), pp. 457–492.

[16] T. G. LIU, B. C. KHOO AND K. S. YEO, *Ghost fluid method for strong shock impacting on material interface*, J. Comput. Phys., 190(2) (2003), pp. 651–681.

[17] C. W. WANG, T. G. LIU AND B. C. KHOO, *A real ghost fluid method for the simulation of multimedium compressible flow*, SIAM J. Sci. Comput., 28(1) (2006), pp. 278–302.

[18] S. K. SAMBASIVAN AND H. S. UDAYKUMAR, *Ghost fluid method for strong shock interactions part 1: Fluid-fluid interfaces*, AIAA J., 47(12) (2009), pp. 2907–2922.

[19] H. TERASHIMA AND G. TRYGGVASON, *A front-tracking/ghost-fluid method for fluid interfaces in compressible flows*, J. Comput. Phys., 228(11) (2009), pp. 4012–4037.

[20] X. Y. HU, B. C. KHOO, N. A. ADAMS AND F. L. HUANG, *A conservative interface method for compressible flows*, J. Comput. Phys., 219(2) (2006), pp. 553–578.

[21] C.-H. CHANG, X. DENG AND T. G. THEOFANOUS, *Direct numerical simulation of interfacial*

instabilities: A consistent, conservative, all-speed, sharp-interface method, J. Comput. Phys., 242 (2013), pp. 946–990.

[22] R. R. NOURGALIEV, M.-S. LIOU AND T. G. THEOFANOUS, *Numerical prediction of interfacial instabilities: Sharp interface method (SIM)*, J. Comput. Phys., 227(8) (2008), pp. 3940–3970.

[23] H. KIM AND M.-S. LIOU, *Adaptive Cartesian sharp interface method for three-dimensional multi-phase flows*, AIAA Paper, (2009), pp. 2009–4153.

[24] W. BO AND J. W. GROVE, *A volume of fluid method based ghost fluid method for compressible multi-fluid flows*, Comput. Fluids, 90 (2014), pp. 113–122.

[25] J. LIN, Y. SHEN, H. DING, N. LIU AND X. LU, *Simulation of compressible two-phase flows with topology change of fluid-fluid interface by a robust cut-cell method*, preparing.

[26] P. L. ROE, *Approximate Riemann solvers, parameter vectors and difference schemes*, J. Comput. Phys., 43 (1981), pp. 357–372.

[27] D. HARTMANN, M. MEINKE AND W. SCHRÖDER, *The constrained reinitialization equation for level set methods*, J. Comput. Phys., 229(5) (2010), pp. 1514–1535.

[28] S. OSHER AND R. FEDKIW, Level Set Methods and Dynamic Implicit Surfaces, Springer, 2003.

[29] A. HARTEN, P. D. LAX AND B. VAN LEER, *On upstream differencing and Godunov-type schemes for hyperbolic conservation laws*, SIAM Rev., 25(1) (1983), pp. 35–61.

[30] C.-W. SHU AND S. OSHER, *Efficient implementation of essentially non-oscillatory shock-capturing schemes*, J. Comput. Phys., 77(2) (1988), pp. 439–471.

[31] R. L. HOLMES, J. W. GROVE AND D. H. SHARP, *Numerical investigation of Richtmyer–Meshkov instability using front tracking*, J. Fluid Mech., 301 (1995), pp. 51–64.

[32] M. A. ULLAH, D.-K MAO AND W.-B. GAO, *Numerical simulations of Richtmyer–Meshkov instabilities using conservative front-tracking method*, Appl. Math. Mech., 32(1) (2011), pp. 119–132.

[33] K. R. BATES, N. NIKIFORAKIS AND D. HOLDER, *Richtmyer–Meshkov instability induced by the interaction of a shock wave with a rectangular block of SF_6*, Phys. Fluids, 19 (2007), 036101.

[34] T. JOHNSEN AND E. COLONIUS, *Shock-induced collapse of a gas bubble in shockwave lithotripsy*, J. Acoust. Soc. Am., 124(4) (2008), pp. 2011–2020.

[35] G. J. BALL, B. P. HOWELL, T. G. LEIGHTON AND M. J. SCHOFIELD, *Shock-induced collapse of a cylindrical air cavity in water: A free-Lagrange simulation*, Shock Waves, 10(4) (2000), pp. 265–276.

[36] X. Y. HU AND B. C. KHOO, *An interface interaction method for compressible multifluids*, J. Comput. Phys., 198(1) (2004), pp. 35–64.

[37] R. R. NOURGALIEV AND T. N. DINH, *Adaptive characteristics-based matching for compressible multifluid dynamics*, J. Comput. Phys., 213(2) (2006), pp. 500–529.

[38] N. A. HAWKER AND Y. VENTIKOS, *Interaction of a strong shockwave with a gas bubble in a liquid medium: A numerical study*, J. Fluid Mech., 701 (2012), pp. 59–97.